



Cite this: *J. Mater. Chem. A*, 2019, 7, 19104

Facile and scalable engineering of a heterogeneous microstructure for uniform, stable and fast lithium plating/stripping†

Xianshu Wang,^a Jingchun Zhuang,^a Mingzhu Liu,^a Cun Wang,^a Yaotang Zhong,^a Huirong Wang,^a Xueqiong Cheng,^a Si Liu,^a Guozhong Cao ^{*b} and Weishan Li ^{*ac}

The uniform, stable and fast lithium (Li) plating/stripping, which enables a Li metal anode to be free from dendrites, is of great importance for the practical application of rechargeable Li metal batteries. Herein, a novel strategy was reported to provide the Li anode with a feature that involved engineering a heterogeneous microstructure on the Li metal *via* the solid-phase reaction between zinc phosphate and Li at room temperature. The as-engineered microstructure consisted of well-distributed LiZn and Li₃PO₄ components, which possessed high Li-ion affinity and provided void spaces, enabling Li plating/stripping to be uniform, stable and fast. The resulting Li anode demonstrated cycling stability values of over 600, 210 and 140 h in an undecorated LiPF₆-based carbonate electrolyte for a symmetric cell at the current densities of 1, 3, and 5 mA cm⁻², respectively, with low voltage hysteresis. Additionally, much better electrochemical performances of LiFePO₄ full batteries could be obtained as compared to that of bare Li. This engineering is facile and scalable for the continuous manufacturing of Li anodes and therefore paves an avenue for the practical application of rechargeable high-energy-density Li metal batteries.

Received 17th June 2019
Accepted 17th July 2019

DOI: 10.1039/c9ta06500h

rsc.li/materials-a

Introduction

Rechargeable batteries with lithium (Li) metal anodes are being significantly pursued for energy-storage applications due to the substantial improvement of storage capacity that outperforms the current state-of-the-art lithium-ion batteries based on a graphite anode.^{1–6} This characteristic is because of not only the high theoretical capacity (3860 mA h g⁻¹) and the most negative potential (−3.04 V, *vs.* standard hydrogen electrode) of the Li metal anode,^{7–10} but also the high accessibility to couple with promising cathodes such as S₈ and O₂.^{11–13} Unfortunately, the fundamental challenges associated with Li plating/stripping on Li metals still remain and perplex researchers. Generally, the Li plating/stripping rate is determined by the convection diffusion of lithium ions (Li⁺) at the electrode/electrolyte interface, where the uneven movement significantly leads to uncontrolled dendritic/powdered/dead Li, which gives rise to volume expansion or even safety hazards.^{14–17} This issue is more

severe at high current densities according to the Sand's equation^{18–21} and inevitably terminates the battery life and causes difficulty to guarantee safe workability.

Considerable tactics for the control of Li plating/stripping have been proposed, and these mainly involve electrode fabrication and artificial interface manufacture. Cui and co-workers fabricated a Li electrode with a polyimide layer, which presented vertical nanoscale channels of a high aspect ratio, and it could disperse the Li⁺ flux uniformly, achieving a uniform Li deposition and dendrite-free surface.¹⁴ Similarly, Xiang *et al.* controlled the diversion of the Li⁺ flux by the modification of a carbon fiber matrix to improve safety.¹⁶ However, the strategies referring to electrode assembly present a significant complexity. An artificial interface armored directly on a Li metal with solid-state electrolyte-like chemistry such as Al₂O₃ and LiF is obviously more facile^{22–26} although such an interface inherently increases the interfacial impedance and enlarges voltage hysteresis.^{25,26} The elevated impedance and hysteresis are highly associated with the lithiophilicity of the architected interface,^{27–34} which regulates the Li plating/stripping processes. Therefore, it is highly desired to rationally design interface chemistry that exhibits high lithiophilicity through a new strategy.

In this contribution, we reported a novel interface design to regulate Li plating/stripping. A heterogeneous microstructure was engineered on a Li metal *via* a facile rolling/grinding process, in which zinc phosphate (Zn₃(PO₄)₂, denoted as ZPO) powder reacted with the Li metal at room temperature (RT). Conveniently, grinding provided extra energy for the occurrence of the

^aSchool of Chemistry and Environment, South China Normal University, Guangzhou 510006, China^bDepartment of Materials Science and Engineering, University of Washington, Seattle, Washington 98195, USA. E-mail: gzc@u.washington.edu^cNational and Local Joint Engineering Research Center of MPTES in High Energy and Safety LIBs, Engineering Research Center of MTEES (Ministry of Education), Key Lab. of ETESPG (GHEI), South China Normal University, Guangzhou 510006, China. E-mail: liwsh@scnu.edu.cn

† Electronic supplementary information (ESI) available. See DOI: 10.1039/c9ta06500h

solid-phase conversion reaction. After conversion, the Li metal surface was engineered with a heterogeneous microstructure that consisted of well-distributed LiZn and Li_3PO_4 particles, which could not only regulate Li plating/stripping but also present low interfacial impedance due to the high lithiophilicity and void spaces provided by the particles. As a result, excellent electrochemical performances were achieved when the well-modulated Li metal (ZPO–Li) anode was tested in symmetric and asymmetric cells. This engineering could also be accomplished for the continuous production of modified Li ribbons under motor driving and therefore is scalable, presenting a great potential for the practical utilization of rechargeable Li metal batteries.

Results and discussion

The basic strategy for engineering a heterogeneous microstructure is illustrated in Fig. 1a. The white ZPO powder insoluble in a carbonate or ether solvent (Fig. S1a and b†) was dispersed onto a fresh Li metal surface. Then, the Li metal was rolled repeatedly until the color of the Li metal surface changed. It could be seen that the silvery surface of the Li metal (Fig. 1b) became black (Fig. 1c) after grinding, indicating the successful engineering of a heterogeneous microstructure *via* the reaction of ZPO with Li metal. Correspondingly, the smooth surface of the fresh Li metal turned into a cragged one, which comprised angular and multi-dimensional particles that were different from those of ZPO (Fig. S1c†). It can be noted from Fig. 1c that the thickness of the microstructure layer is $\sim 10\ \mu\text{m}$, which consists of Li_3PO_4 , LiZn

and $\text{Zn}_3(\text{PO}_4)_2$, as confirmed below. The loading amount of these species was $\sim 1.4\ \text{g cm}^{-2}$, which was determined by weighing the residues after dissolving the sample in alcohol. Reducing the loading amount of $\text{Zn}_3(\text{PO}_4)_2$ could not ensure the uniform coverage of the microstructure layer on the Li metal. Under the cross-sectional view, the particles in the resulting microstructure could be identified by SEM and their composition could be confirmed by elemental mappings (Fig. S2†), which were different from those of bare Li (inset SEM images in Fig. 1b). Furthermore, TEM characterizations showed the sizes and polycrystalline lattices of sub-particles as well as the heterogeneous microstructure (Fig. S3†). This morphological evolution after rolling was attributed to the solid-phase conversion, which could be confirmed by the Gibbs free energy change (Fig. S4†). The much negative Gibbs free energy change ($\Delta G = -1495\ \text{kJ mol}^{-1}$) verified the feasibility of the solid-phase conversion reaction: $\text{Zn}_3(\text{PO}_4)_2 + 9\text{Li} = 2\text{Li}_3\text{PO}_4 + 3\text{LiZn}$. X-ray diffraction (XRD) patterns were recorded to characterize the formed species on a Li foil after conversion (Fig. 1d). After the conversion reaction, many peaks of ZPO powder disappeared and were replaced by the weak (110) and (101) peaks of Li_3PO_4 , the strong (111), (220) and (311) peaks of LiZn and some residual ZPO peaks in addition to the main (110) peak of Li metal. This weak Li_3PO_4 signal could be explained by the amorphous structure of Li_3PO_4 formed from solid-phase conversion. These featured surface components were further validated by the X-ray photoelectron (XPS) analysis of the ZPO powder and ZPO–Li (Fig. 1e, f and S5†). The new peaks appearing at low binding

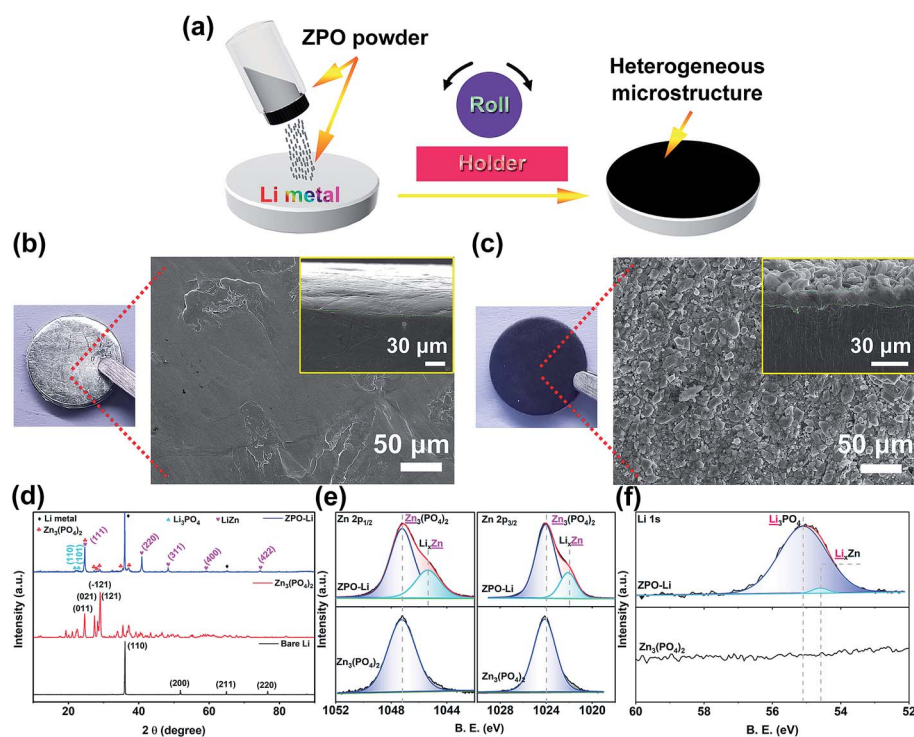


Fig. 1 (a) Schematic illustration of rolling operation for generating the heterogeneous microstructure on Li metal. Digital photos and top-view and cross-sectional SEM images of Li foil (b) before and (c) after rolling. (d) XRD patterns of bare Li, ZPO powder and ZPO–Li. The (e) Zn 2p and (f) Li 1s XPS spectra of pure ZPO powder and ZPO–Li.

energies in the Zn 2p_{3/2} and Zn 2p_{1/2} spectra of ZPO–Li (Fig. 1e) suggest that the ZPO–Li electrode contains another Zn-based species that is different from ZPO.^{35–37} This species presented slightly lower binding energy than that of a pure Zn metal (1022.3 eV),³⁸ indicating the formation of a Li_xZn alloy. The electron density of Li shifted to Zn due to the different electronegativities, resulting in the decreased binding energy of Zn in the formed alloy. This alloy phase was also detected in the Li 1s spectrum of ZPO–Li (54.6 eV, Fig. 1f). Moreover, a highly obvious peak at 55.1 eV corresponding to Li₃PO₄ (ref. 39) could be identified in the Li 1s spectrum of ZPO–Li. The dissimilarities between the P 2p and O 1s spectra (Fig. S5†) further confirmed the formation of Li₃PO₄ after rolling.

To understand the effect of surface components on Li plating/stripping, the Vienna *ab initio* simulation package (VASP) and Gaussian 09 package were used to simulate the Li affinity and chemical stabilities (Fig. 2). As shown in Fig. 2a and b, the (111) and (220) planes of the LiZn alloy deliver binding energies of -2.30 and -2.16 eV, respectively. Both are more negative than that of the (111) plane of Li metal (-1.58 eV) (Fig. 2c), indicating the high Li affinity of LiZn that is beneficial for the on-surface diffusion of Li atoms during plating/stripping.²⁹ Furthermore, the Li₃PO₄ component stabilized the Li metal due to the differences between their energy levels (Fig. 2d). The highest occupied molecular orbital (HOMO) energy of Li metal is inferior to that of the lowest unoccupied molecular orbital (LUMO) of Li₃PO₄, providing an insurmountable gap for electrons. Thus, Li₃PO₄ can maintain the interfacial stability by preventing the Li metal degradation and electrolyte depletion. In addition, Li₃PO₄ also guarantees fast on-surface diffusion during Li plating/stripping due to its ion conductivity.⁴⁰ These features endowed the as-engineered heterogeneous microstructure with the ability to regulate homogenized, stabilized and fast Li plating/stripping (Fig. 2e).

In contrast, the bare Li anode suffered from the locally dense Li⁺ flux and serious electrolyte decomposition, leading to dendrite growth, electrode pulverization and volume expansion (Fig. 2f).

To evaluate the electrochemical performance of ZPO–Li, symmetric cells with bare Li or ZPO–Li electrodes were fabricated and then charged/discharged by the galvanostatic mode in the undecorated LiPF₆-EC/EMC/DMC electrolyte (Fig. 3). At current density of 1 mA cm⁻² with controlled Li plating/stripping capacity (1 mA h cm⁻²), the symmetric cell with bare Li rendered fast increment in voltage hysteresis after 100 cycles, which exceeded the axis range at 260 h (Fig. 3a). This very high voltage increase resulted from the increased resistance by the accumulation of the by-products of electrolyte decomposition and “dead Li”.⁴¹ In contrast, much smaller voltage fluctuation and increase during the cycling over 600 h were detected for the ZPO–Li-based symmetric cell. This voltage fluctuation and increase were still present for the ZPO–Li-based cell, but they were smaller than that of the bare Li-based cell, suggesting that the electrolyte decomposition is inevitable on the ZPO–Li electrode. The optimization of electrolyte components further highlights the boosted cyclic lifespan of Li plating/stripping by the as-engineered heterogeneous microstructure (Fig. S6†). The electrolyte additive was responsible for stable cycling over 600 h for the bare Li electrode, but voltage increase was inevitable for the subsequent cycling. After cycling over 820 h, the ZPO–Li electrode remained stable without voltage undulation and short-circuit. The contribution of the as-engineered heterogeneous microstructure became more obvious at higher current densities. When the current density increased to 3 mA cm⁻² (Fig. 3b), the ZPO–Li cell showed a consistent and stable plateau overpotential for Li plating/stripping and no cell short-circuit during the whole cycling lifetime (210 h); in contrast, the bare Li-based cell maintained stable cycling of less than 80 h and exhibited a short-circuit indicated by the appearance of

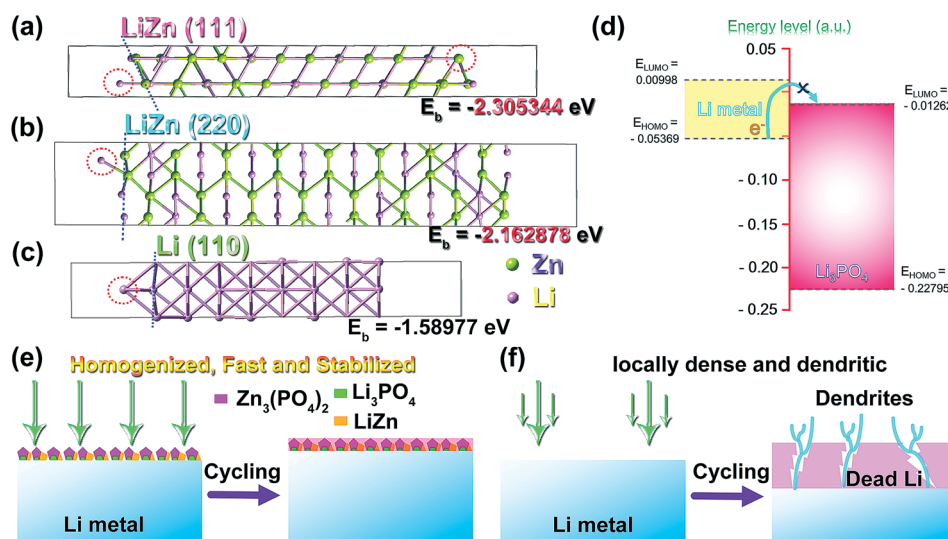


Fig. 2 The binding energy of (a) (111) and (b) (220) planes of LiZn and (c) (110) plane of Li metal with Li atom. (d) Energy level comparison of frontier molecule orbital of Li metal and Li₃PO₄, verifying the stability of Li₃PO₄ component. (e and f) Schematic diagrams of Li depositing on Li anodes with and without heterogeneous microstructure.

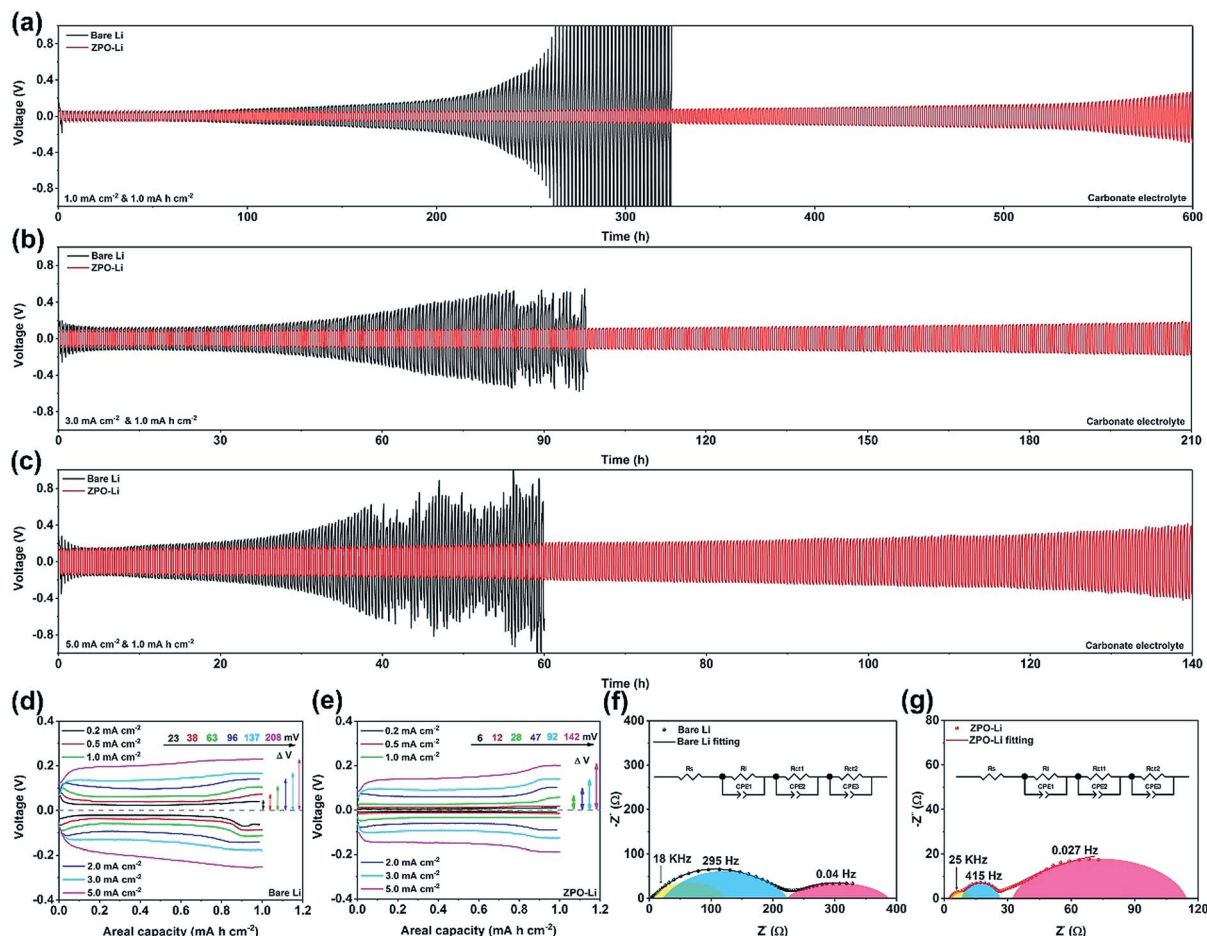


Fig. 3 Electrochemical performances of the ZPO-Li anode. The cycling stability of symmetric cells using bare Li and ZPO-Li electrodes at various current densities of (a) 1.0, (b) 3.0 and (c) 5.0 mA cm⁻² with a Li plating/stripping capacity of 1.0 mA h cm⁻². Voltage-areal capacity profiles of symmetric cells with (d) bare Li and (e) ZPO-Li electrodes at different current densities of 0.2, 0.5, 1, 2, 3 and 5 mA cm⁻². Electrochemical impedance spectra of symmetric cells with (f) bare Li and (g) ZPO-Li electrodes after 3 cycles. Insets in (f) and (g) are the equivalent circuit for fitting.

anomalous voltage rising and falling at the 130th cycle due to the formation of Li dendrites. It should be noted that the size modulation of the Zn₃(PO₄)₂ particles played an important role in the cyclability of the ZPO-Li electrode (Fig. S7[†]). At 5 mA cm⁻², the ZPO-Li cell significantly predominated in cyclic stability as compared to the short-lived bare Li cell (140 vs. 40 h, Fig. 3c). When the current density was controlled to 1.0 mA cm⁻² with fixed capacity of 3.0 mA h cm⁻², the different life-spans and overpotentials of the symmetric cells revealed the superior stability (Fig. S8[†]). These results demonstrate that the ZPO-derived heterogeneous microstructure can serve as a good candidate to boost the Li anode.

To evaluate the characteristics of ZPO-Li, the correlation between voltage hysteresis and current densities and the electrochemical impedance was evaluated and analyzed in detail. As shown in Fig. 3d, the bare Li symmetric cell exhibits pronounced polarization voltages of 23, 98 and 208 mV at the current densities of 0.2, 2.0 and 5.0 mA cm⁻², respectively. In contrast, a smaller voltage hysteresis increment from 6 to 142 mV at the corresponding current densities was observed for the symmetric

cell with ZPO-Li electrodes (Fig. 3e). These values were lower than the de-lithiation potential of the LiZn alloy (0.27 V vs. Li/Li⁺), suggesting that the de-alloying process of the LiZn component did not occur during the Li stripping stage for the ZPO-Li symmetric cell. The enhanced anti-current capability was attributed to the reduced real current density and the regulated Li plating/stripping by the as-engineered heterogeneous microstructure. The electrochemical impedance spectra of the symmetric cells after 3 cycles are presented in Fig. 3f and g. Here, the as-tested dots can be fitted through the equivalent circuit (insets in Fig. 3f and g), as shown by the fitting lines. There are three arcs for both bare Li and ZPO-Li cells after the fitting. According to a previous report,⁴² the first semicircle in the high-frequency region reflects the effect of the interface layer ($R_{i,bulk}$), and the other two arcs involve the charge transfer resistance ($R_{A/I}$ and $R_{E/I}$; here, A, E and I represent anode, electrolyte and interface, respectively), as schematically depicted in Fig. S9a.† The bare Li-based cell presented a high $R_{i,bulk}$ value of 144.5 Ω (Fig. S9b.†), corresponding to the yellow area in Fig. 3f, indicating the poor Li⁺ kinetics at the bare Li electrode resulting

from the deteriorated interface under pre-formation. In comparison, a low interface resistance of 5.2Ω was obtained for the ZPO–Li electrode (yellow area in Fig. 3g), indicating the fast Li deposition/dissolution due to the contribution of the as-engineered heterogeneous microstructure. Moreover, the much lower $R_{A/I}$ value (15.4Ω) of the ZPO–Li electrode (cyan arc in Fig. 3g) than that of the bare Li electrode (155.3Ω , cyan arc in Fig. 3f) indicated the good lithophilicity of LiZn and the high Li^+ conductivity of Li_3PO_4 ,⁴⁰ suggesting that Li^+ can be easily reduced with expedited electron transfer underneath the interface. In contrast, $R_{E/I}$ shows the opposite case (rosy arcs, 134.8Ω vs. 88.9Ω), which can be attributed to the anti-reducibility and stability of Li_3PO_4 . Apparently, the as-engineered heterogeneous microstructure was effectively responsible for the circumvention of electrolyte decomposition and decrease in the plating/stripping overpotential and the cell resistance. The electrochemical impedance spectra of the cells with different cycles further confirmed the improved stability of the ZPO–Li electrode by the heterogeneous microstructure (Fig. S10†).

SEM was conducted to compare the surface and cross-section morphologies of the bare Li and ZPO–Li electrodes. The morphological evolution of the bare Li and ZPO–Li surfaces can be illustrated in Fig. 4a and b. The top-view of bare Li after 1st plating displays multiple filament-consisted cakes with random distribution (Fig. 4c), which results from the poor SEI-induced irregular Li^+ flux.⁴³ During 1st stripping, the plated Li could not return to the counter electrode due to the blocking

from SEI. Instead, bulk Li dissolved, rendering some pores on the Li surface (Fig. 4d). The as-engineered heterogeneous microstructure was a mixed conducting layer based on the electronic conductor of LiZn and Li^+ conductor of Li_3PO_4 . Additionally, the more negative binding energy of LiZn caused a faster movement of Li^+ to LiZn sites. Therefore, the ZPO–Li electrode displayed uniform Li plating in the as-engineered heterogeneous microstructure (Fig. S11†), resulting in smooth morphology (Fig. 4e). This feature is associated with the high surface area-reduced current density and the wettability of the LiZn component. With regard to 1st stripping, the ZPO–Li electrode recovered to particle-covered surface morphology (Fig. 4f), suggesting reversible Li plating/stripping. The digital photographs of the bare Li and ZPO–Li electrodes after 1st plating and stripping further confirm that the ZPO-derived heterogeneous microstructure possesses uniform Li depositing/stripping on the whole surface rather than the local and random one of the bare Li electrode (Fig. S12†).

With further cycling, the surface of bare Li deteriorated seriously, as shown in Fig. 4g–i. The cross-sectional SEM image of the bare Li electrode after 10 cycles afforded an incompact layer of “dead Li” ($23 \mu\text{m}$, Fig. 4g). Worse still, this notorious layer expanded by 17% and 104% after 20 and 40 cycles, respectively (Fig. 4h and i). Their respective top-view SEM images further confirm the serious deterioration of the bare Li electrode, presenting dendrite growth, dead Li micro-particles, electrolyte byproducts and interbedded cracks (insets in

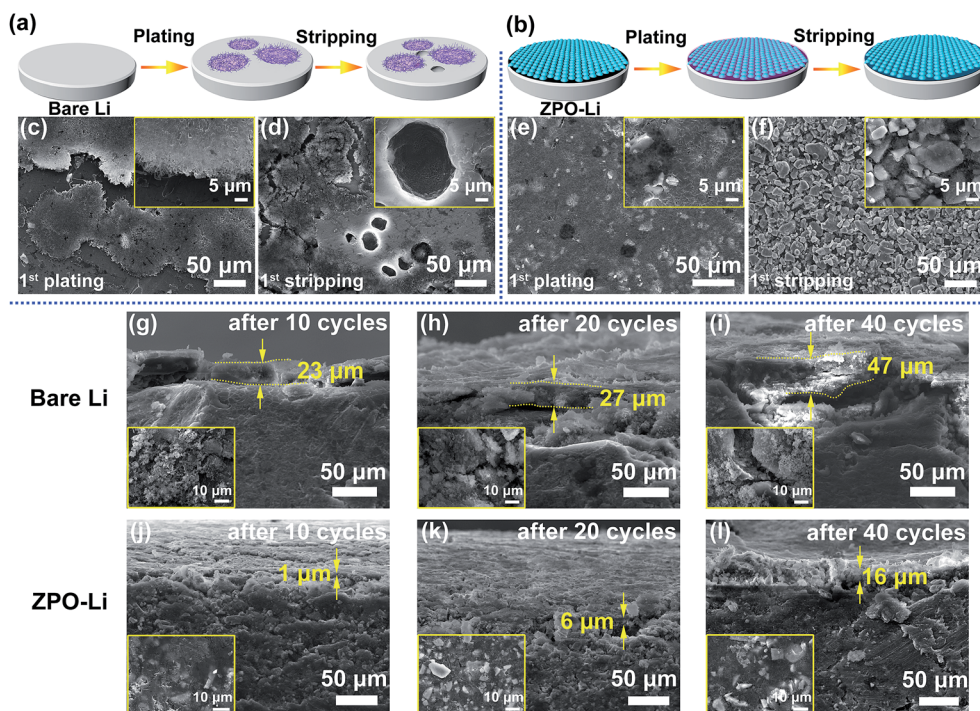


Fig. 4 Structure and morphology of bare Li and ZPO–Li anodes after cycling at a current density of 1.0 mA cm^{-2} . Schematic illustration of the Li plating/stripping behavior of (a) bare Li and (b) ZPO–Li electrodes. Top-view SEM images of (c and d) bare Li and (e and f) ZPO–Li electrodes after 1st (c and e) plating and repeated (d and f) plating/stripping. Insets in (c–f) are the respective enlarged views at local. Cross-sectional SEM images of (g–i) bare Li and (j–l) ZPO–Li electrodes after (g and j) 10, (h and k) 20, and (i and l) 40 cycles in the discharged state. Insets in g–l are the corresponding top-view SEM images.

Fig. 4g–i). Fortunately, the ZPO–Li electrode effectively circumvented these issues, maintaining a smooth and dendrite-free surface after deep cycling (inset top-view SEM images in Fig. 4j–l). Under a cross-sectional view, we observed that the ZPO–Li electrode after 10 cycles displayed negligible volume expansion without obvious layer separation (Fig. 4j), which was maintained up to 20 cycles (Fig. 4k). After 40 cycles, only a slight increase in the surface layer thickness occurred (Fig. 4l). These observations emphasized that volume expansion and dendrite growth as well as electrolyte side reactions are highly suppressed by the as-engineered heterogeneous microstructure. Therefore, a very smooth and integrated surface could be observed on the ZPO–Li electrode compared to the uneven one on the bare Li electrode (Fig. S13†).

To demonstrate the alternative large-scale energy-storage applications of Li metal batteries, a high-safety and long-lifespan lithium iron phosphate (LiFePO_4 , 6.5 mg cm^{-2} , 1.0 mA h cm^{-2} Li capacity) cathode was selected for coupling with Li anodes (Fig. 5). Fig. 5a presents the long-term cyclic performances of $\text{Li}||\text{LiFePO}_4$ full batteries with different Li anodes, which delivered very different capacities. The bare $\text{Li}||\text{LiFePO}_4$ battery offered initial specific capacity of 130 mA h g^{-1} at a rate of 1C ($1\text{C} = 170 \text{ mA g}^{-1}$); it presented fast capacity decay after 177 cycles and possessed discharge capacity of only 56.7 mA h g^{-1} with capacity retention of 44% after 250 cycles. In contrast, slightly higher specific capacity of 135 mA h g^{-1} at the initial cycle was obtained for the ZPO–

$\text{Li}||\text{LiFePO}_4$ battery due to the reduced interfacial resistance by the as-engineered microstructure. After 300 cycles, capacity of 85 mA h g^{-1} (64% of the initial capacity) remained. The voltage–capacity profiles at the selected cycles also confirmed the significantly improved cyclic stability of the ZPO–Li $||\text{LiFePO}_4$ battery (Fig. S14†). Moreover, the ZPO–Li $||\text{LiFePO}_4$ battery also presented better rate capability than the $\text{Li}||\text{LiFePO}_4$ battery (Fig. 5b). The ZPO–Li $||\text{LiFePO}_4$ battery contributed to the reversible capacities of 153.8, 142.4, 128.9, 113.5, and 95.6 mA h g^{-1} at 0.2, 0.5, 1, 2, and 4C, respectively. In contrast, only 151.8, 137.3, 122.7, 107, and 85.5 mA h g^{-1} were obtained for the bare $\text{Li}||\text{LiFePO}_4$ battery under the same conditions due to sluggish kinetics. As demonstrated in Fig. 5c–e, the bare $\text{Li}||\text{LiFePO}_4$ battery presents larger interfacial resistance than the ZPO–Li $||\text{LiFePO}_4$ battery under various states: before cycling, after 3 cycles, and after 20 cycles. Such a distinct feature yielded difference in polarizations between discharge and charge curves (123 vs. 78 mV) and the initial charging stage (3.536 vs. 3.473 V) for the two batteries (Fig. S15†). For the battery with the ZPO–Li anode, the interfacial resistance remained unchanged from initial to 20 cycles, signifying its excellent stability. The surface of bare Li was coated with a dark layer (Fig. 5f), and its color changed from gray to dark, resulting from the self-ignition of the high-specific-surface Li microparticles and electrolyte side-products in the glove box. Under magnified SEM, many particles with various sizes can be observed with free scattering. Moreover, there appeared several

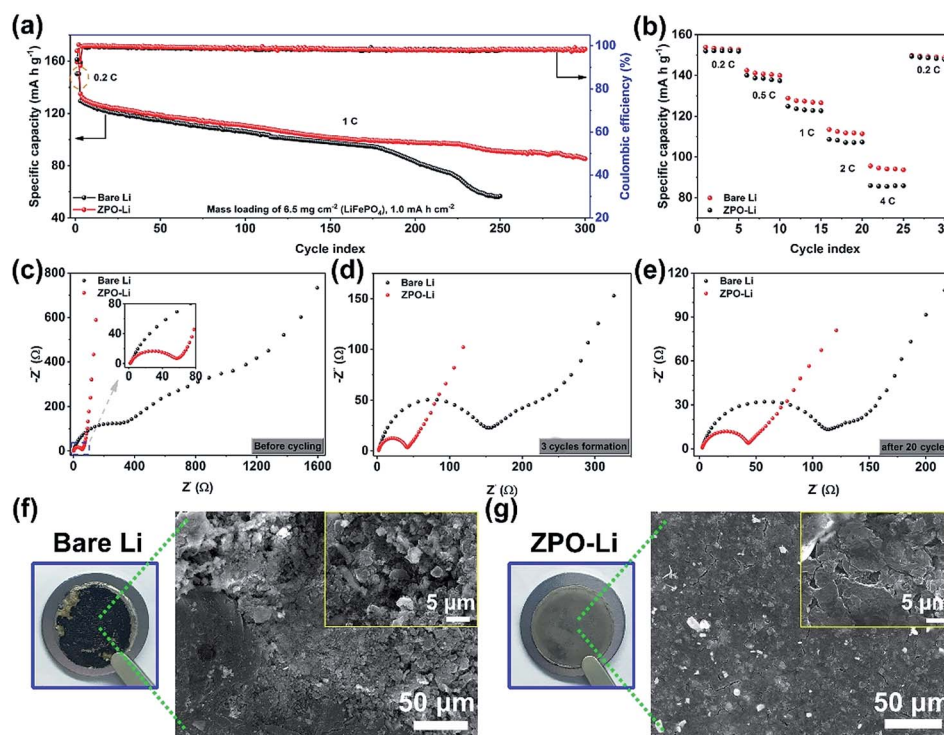


Fig. 5 (a) Galvanostatic cycling performance at a rate of 1C ($1\text{C} = 170 \text{ mA g}^{-1}$) and (b) rate capability at different rates from 0.2 to 4C for bare $\text{Li}||\text{LiFePO}_4$ and ZPO–Li $||\text{LiFePO}_4$ full batteries. The electrochemical impedance spectra of bare $\text{Li}||\text{LiFePO}_4$ and ZPO–Li $||\text{LiFePO}_4$ batteries (c) before cycling, after (d) 3 cycle formation and (e) 20 cycles. The digital photos and SEM images of (f) bare Li and (g) ZPO–Li anodes after cycling in LiFePO_4 -based batteries. Insets in SEM images of f and g are the local enlarged view.

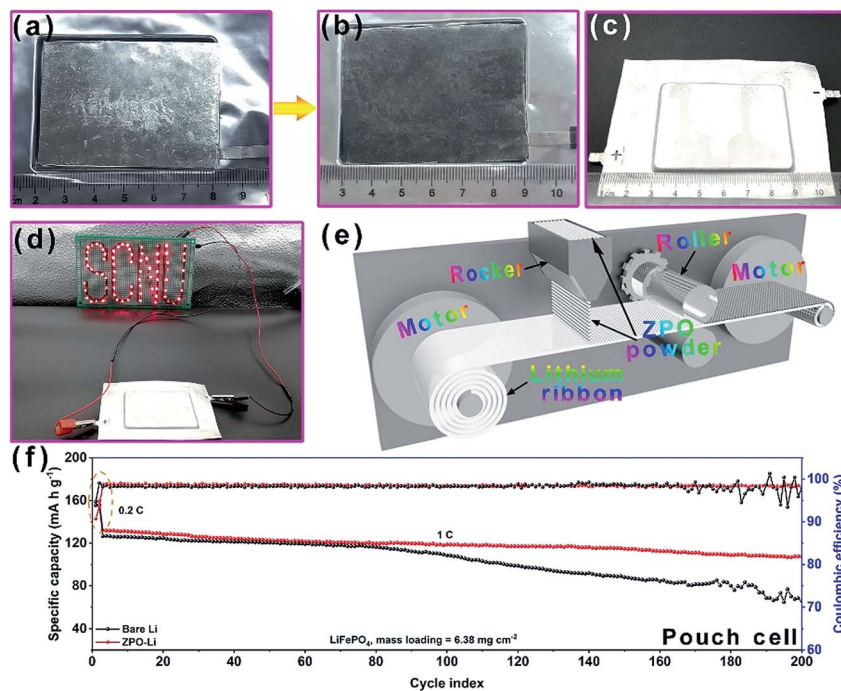


Fig. 6 Schematic drawing of scalable rolling and pouch cell presenting LiFePO_4 -based battery with ZPO-Li anode. Optical images of large-scale Li ribbon (a) before and (b) after rolling ZPO powder. (c) Optical image of the pouch cell with ZPO-Li anode. (d) The "SCNU" typeface lit by a string of lights containing 77 light emitting diodes (LEDs). (e) Schematic drawing of a roll-to-roll system for the continuous flow production of ZPO-Li anodes. (f) The long-term galvanostatic cyclability of the LiFePO_4 -based pouch cells with the yielded ZPO-Li and bare Li ribbons.

holes with different sizes and depths, resulting from the "dead Li" formation and pulverization by electrolyte infringement. In contrast, the ZPO-Li anode preserved its surface integrity without dendrite growth (Fig. 5g), but some small crevices were present; these were associated with the uneven byproduct accumulation from the inevitable electrolyte decomposition when we performed deep cycling for the Li electrode. Similar electrochemical performances and surface morphologies can also be seen for lithium-free $\text{Li}_4\text{Ti}_5\text{O}_{12}$ -based full batteries (Fig. S16–S18[†]), further evidencing the greatly improved cyclability, reduced ion transport barrier and dendrite-free behavior upon cycling in the presence of ZPO-Li anodes. All these improved characteristics were ascribed to the as-engineered heterogeneous microstructure after rolling: (a) excellent Li wettability, (b) uniformly decentralized Li^+ flux, and (c) retentive interfacial stability with low resistance.

As an additional advantage of this extremely facile strategy, the scalable production of dendrite-free Li anodes could be achieved in spite of the existing huge challenges. As shown in Fig. 6, a Li ribbon (length 60 mm \times width 48 mm, Alfa aesar, 99.9%) can be successfully implemented. The surface color changed from silvery to black after repeated rolling (Fig. 6a and b). Furthermore, a large type of LiFePO_4 cathode (mass loading, 6.38 mg cm^{-2} ; length, 57 mm \times width 45 mm, Fig. S19[†]) was paired with the scale-up ZPO-Li anode to fabricate a pouch cell (Fig. 6c), which successfully lit the "SCNU" typeface composed of 77 light-emitting diodes (LEDs) after charging (Fig. 6d). Fig. 6e shows the schematic illustration of a roll-to-roll system for the continuous production of the ZPO-Li anode. The motors

drove the Li ribbon to coil at an adjustable speed within a certain tension; meanwhile, the reactant powder was scattered by a tuned shaker. Then, Li ribbons passed through the press-tunable roller to be ground for the solid-phase conversion reaction. The continuous and scale-up manufacturing of the ZPO-Li anode could be combined in a roll-to-roll system, which was similar to the currently prevailing pre-lithiation technology. Furthermore, after being coupled with the LiFePO_4 cathode, the modified Li anode was fabricated to measure its usability in practice. High capacity retention and stable coulombic efficiency (CE) of the ZPO-Li|| LiFePO_4 pouch cell against the dendrite-induced low retention and fluctuated CE in the bare Li|| LiFePO_4 pouch cell were detected within 200 cycles at a rate of 1C (Fig. 6f). These results demonstrated that the strategy developed in this work is feasible for the practical applications of Li metal anodes.

Conclusions

A convenient rolling ZPO powder to react with Li at room temperature was successfully developed, yielding a heterogeneous microstructure on a Li metal. The as-engineered heterogeneous microstructure featured lithiophilicity and stability, which originated from the derived LiZn and Li_3PO_4 components, enabling the fast Li plating/stripping to be uniform and stable. As a result, enhanced cyclic lifespan and rate capability for the Li||Li symmetric cell were obtained with a low overpotential and interfacial resistance, enhanced anti-current capability, lower volume expansion, and the absence of

dendrite growth. The modified Li anode was also superior to the bare Li anode with respect to the electrochemical performance of the LiFePO₄-based full batteries. Impressively, a scalable model was designed to produce large-scale and dendrite-free Li anodes with feasible continuity by motor driving, powder coverage, and rolling technique. Our facile strategy can be further extended to other reactants and also emphasizes the potential commercialization for high-safety and long-lifespan Li metal batteries.

Conflicts of interest

There are no conflicts to declare.

Acknowledgements

This work is financially supported by the National Key Research and Development Program of China (Grant No. 2018YFB0104000), the Key Project of Science and Technology in Guangdong Province (Grant No. 2017A010106006).

Notes and references

- X. B. Cheng, R. Zhang, C. Z. Zhao and Q. Zhang, *Chem. Rev.*, 2017, **117**, 10403–10473.
- D. Lin, Y. Liu and Y. Cui, *Nat. Nanotechnol.*, 2017, **12**, 194–206.
- Y. Guo, H. Li and T. Zhai, *Adv. Mater.*, 2017, **29**, 1700007.
- X. Shen, H. Liu, X.-B. Cheng, C. Yan and J.-Q. Huang, *Energy Storage Materials*, 2018, **12**, 161–175.
- L. Lin, F. Liang, K. Zhang, H. Mao, J. Yang and Y. Qian, *J. Mater. Chem. A*, 2018, **6**, 15859–15867.
- L. Wang, Z. Zhou, X. Yan, F. Hou, L. Wen, W. Luo, J. Liang and S. X. Dou, *Energy Storage Materials*, 2018, **14**, 22–48.
- Z. A. Ghazi, Z. Sun, C. Sun, F. Qi, B. An, F. Li and H. M. Cheng, *Small*, 2019, 1900687.
- B. Liu, J.-G. Zhang and W. Xu, *Joule*, 2018, **2**, 833–845.
- R. Cao, W. Xu, D. Lv, J. Xiao and J.-G. Zhang, *Adv. Energy Mater.*, 2015, **5**, 1402273.
- S. Li, M. Jiang, Y. Xie, H. Xu, J. Jia and J. Li, *Adv. Mater.*, 2018, **30**, 1706375.
- Z. Lin and C. Liang, *J. Mater. Chem. A*, 2015, **3**, 936–958.
- Y. He, Z. Chang, S. Wu and H. Zhou, *J. Mater. Chem. A*, 2018, **6**, 6155–6182.
- H. Song, H. Deng, C. Li, N. Feng, P. He and H. Zhou, *Small Methods*, 2017, **1**, 1700135.
- W. Liu, D. Lin, A. Pei and Y. Cui, *J. Am. Chem. Soc.*, 2016, **138**, 15443–15450.
- X. B. Cheng, T. Z. Hou, R. Zhang, H. J. Peng, C. Z. Zhao, J. Q. Huang and Q. Zhang, *Adv. Mater.*, 2016, **28**, 2888–2895.
- J. Xiang, L. Yuan, Y. Shen, Z. Cheng, K. Yuan, Z. Guo, Y. Zhang, X. Chen and Y. Huang, *Adv. Energy Mater.*, 2018, **8**, 1802352.
- M.-H. Ryou, D. J. Lee, J.-N. Lee, Y. M. Lee, J.-K. Park and J. W. Choi, *Adv. Energy Mater.*, 2012, **2**, 645–650.
- X.-B. Cheng and Q. Zhang, *J. Mater. Chem. A*, 2015, **3**, 7207–7209.
- W. Xu, J. Wang, F. Ding, X. Chen, E. Nasybulin, Y. Zhang and J.-G. Zhang, *Energy Environ. Sci.*, 2014, **7**, 513–537.
- D. Wang, W. Zhang, W. Zheng, X. Cui, T. Rojo and Q. Zhang, *Adv. Sci.*, 2017, **4**, 1600168.
- H. E. Park, C. H. Hong and W. Y. Yoon, *J. Power Sources*, 2008, **178**, 765–768.
- A. C. Kozen, C. F. Lin, A. J. Pearse, M. A. Schroeder, X. Han, L. Hu, S. B. Lee, G. W. Rubloff and M. Noked, *ACS Nano*, 2015, **9**, 5884–5892.
- F. Liu, Q. Xiao, H. B. Wu, L. Shen, D. Xu, M. Cai and Y. Lu, *Adv. Energy Mater.*, 2018, **8**, 1701744.
- E. Kazyak, K. N. Wood and N. P. Dasgupta, *Chem. Mater.*, 2015, **27**, 6457–6462.
- W. Wang, X. Yue, J. Meng, J. Wang, X. Wang, H. Chen, D. Shi, J. Fu, Y. Zhou, J. Chen and Z. Fu, *Energy Storage Materials*, 2019, **18**, 414–422.
- L. Fan, H. L. Zhuang, L. Gao, Y. Lu and L. A. Archer, *J. Mater. Chem. A*, 2017, **5**, 3483–3492.
- G. Huang, J. Han, F. Zhang, Z. Wang, H. Kashani, K. Watanabe and M. Chen, *Adv. Mater.*, 2019, **31**, 1805334.
- P. Shi, T. Li, R. Zhang, X. Shen, X. B. Cheng, R. Xu, J. Q. Huang, X. R. Chen, H. Liu and Q. Zhang, *Adv. Mater.*, 2019, **31**, e1807131.
- X. Wang, Z. Pan, Y. Wu, X. Ding, X. Hong, G. Xu, M. Liu, Y. Zhang and W. Li, *Nano Res.*, 2018, **12**, 525–529.
- X. Wang, Z. Pan, Y. Wu, G. Xu, X. Zheng, Y. Qiu, M. Liu, Y. Zhang and W. Li, *Nanoscale*, 2018, **10**, 16562–16567.
- C. Sun, Y. Li, J. Lin, J. Yang and Z. Wen, *J. Mater. Chem. A*, 2019, **7**, 7752–7759.
- C. Zhang, W. Lv, G. Zhou, Z. Huang, Y. Zhang, R. Lyu, H. Wu, Q. Yun, F. Kang and Q.-H. Yang, *Adv. Energy Mater.*, 2018, **8**, 1703404.
- Y. Liu, D. Lin, Z. Liang, J. Zhao, K. Yan and Y. Cui, *Nat. Commun.*, 2016, **7**, 10992.
- Z. Liang, D. Lin, J. Zhao, Z. Lu, Y. Liu, C. Liu, Y. Lu, H. Wang, K. Yan, X. Tao and Y. Cui, *Proc. Natl. Acad. Sci. U. S. A.*, 2016, **113**, 2862–2867.
- R. Zeng, Y. Hu, F. Zhang, Y. Huang, Z. Wang, S. Li and E. Han, *Trans. Nonferrous Met. Soc. China*, 2016, **26**, 472–483.
- D. L. Felker and P. M. A. Sherwood, *Surf. Sci. Spectra*, 2002, **9**, 106–113.
- O. Lupan, G. A. Emelchenko, V. V. Ursaki, G. Chai, A. N. Redkin, A. N. Gruzintsev, I. M. Tiginyanu, L. Chow, L. K. Ono, B. Roldan Cuenya, H. Heinrich and E. E. Yakimov, *Mater. Res. Bull.*, 2010, **45**, 1026–1032.
- S. Feliu and V. Barranco, *Acta Mater.*, 2003, **51**, 5413–5424.
- A. T. Appapillai, A. N. Mansour, J. Cho and Y. Shao-Horn, *Chem. Mater.*, 2007, **19**, 5748–5757.
- N. W. Li, Y. X. Yin, C. P. Yang and Y. G. Guo, *Adv. Mater.*, 2016, **28**, 1853–1858.
- K.-H. Chen, K. N. Wood, E. Kazyak, W. S. LePage, A. L. Davis, A. J. Sanchez and N. P. Dasgupta, *J. Mater. Chem. A*, 2017, **5**, 11671–11681.
- M. R. Busche, T. Drossel, T. Leichtweiss, D. A. Weber, M. Falk, M. Schneider, M. L. Reich, H. Sommer, P. Adelhelm and J. Janek, *Nat. Chem.*, 2016, **8**, 426–434.
- H. Yang, C. Guo, A. Naveed, J. Lei, J. Yang, Y. Nuli and J. Wang, *Energy Storage Materials*, 2018, **14**, 199–221.